Multi-dimensional numerical modelling of heavy ion transport in matter using a fast and accurate method

Thanh-Ha Nguyen-Bui, Alexandre Larouze, Rémi Bourgeois, Bruno Dubroca

Multi-dimensional numerical modelling of heavy ion transport in matter using a fast and accurate method

Thanh-Ha Nguyen-Bui[1], **Alexandre Larouze, Rémi Bourgeois**
CELIA, UMR 5107, Université de Bordeaux – CNRS – CEA,
351, Cours de la Libération, 33405 Talence, France

Bruno Dubroca
LCTS, CNRS – CEA – Safran,
3 Allée de la Boétie, 33600 Pessac, France

Abstract

Simulations of ion slowing-down beams in thick targets aim at characterizing the spatial and energy distributions of incident ions inside the matter. However, to simulate the propagation of a heavy ion beam we must confront several difficulties due to the stiffness of physical phenomena. In this paper, we propose to develop a moment method with a high order accuracy numerical scheme to solve the Fokker-Planck equation. The algorithm is accurate and fast enough to be used in operational processes of dose deposition optimization. Several benchmarks are carried out and will be presented in this paper.

Keyword : Heavy ion transport, Moment Method, Numerical Scheme, High Order Accuracy, Realizability.

1 Introduction

Until the middle of the past century, penetration of charged-particle were stimulated almost exclusively for the needs of fundamental physics research, but the applications in other areas gradually became important. Quantitative information on the penetration of charged ions through matter, in particular the energy loss, is of considerable interest in basic science, medicine and technology. For example, the presence of heavy ions in the galactic cosmic rays (GCR) has been observed at high altitude in the Earth's atmosphere (Freier *et al.*, 1948 [1]). Recently, the use of accelerated heavy ions has been proved fruitful for the exploration of the structures of unstable states of atomic nuclei as well as the multiple nuclear reactions that which occur in stars, supernovae [2] and also between matter and cosmic radiation [3]. Continuing this research on the origins and properties of nuclear matter requires the use of beams of unstable nuclei with a large excess of protons or neutrons. These methods require very intense ion sources (protons, deuterons, more or less heavy ions obtained by the combined action of electric and magnetic fields to ionize and gathered the ions. The progress achieved in the generation of ion sources benefits all kind accelerator facilities, from small cyclotrons intended to destroy tumors by ion beams (proton therapy [4], radiotherapy with carbon ions [5]) to those which produce medical and industrial isotopes. The development of increasingly efficient and reliable accelerators is providing particle beams with properties virtually on demand. It is now possible to use them to irradiate targets of all kinds. The target can be a malignant tumor to be treated (medical sector [6]), a food to be sterilized (food safety sector [7]), or even a spallation target intended to produce neutrons (scientific research sector [8]).

Some biology effects are caused by energy deposition, which may be accurately calculated with Monte Carlo codes. However, solving directly the system of linear transport equations for the motion of particles is computationally expensive, and thus nowadays incompatible with practical

[1]thanh-ha.nguyen-bui@u-bordeaux.fr

applications. The moment method, used in a very large of physical applications [9, 10, 11, 12, 13] consists in replacing the linear Boltzmann transport equation by a reduced number of moment equations of lower dimension. Such an approach allows to reduce the number of degrees of freedom, i.e. the number of variables, saving memory space and a significant amount of computations while maintaining a satisfying accuracy. The moments method has already been used by some authors for the propagation of electrons in matter [14, 15, 16].

This study focuses on the propagation of ions. Simulations of slowing-down of ion beams in thick targets aim at characterizing the spatial and energy distributions of incident particles and secondary fragments in matter. Quantitative physics, including the energy deposited (dose), on the penetration of ions through matter represents a fundamental aspect for a wide diversity of applications: the development of new materials for devices able to work in hostile conditions (high fields of radiation, extreme temperature or pressure), new principles and techniques of detection, reactor waste technologies, medical applications, dosimetry, etc. The great difference between electrons and ions is that unlike electrons, the deflection of ions when colliding with molecules is almost zero, since the mass of the ions is much more important. So almost all beam energy is deposited at the end of the ion path before stopping abruptly. This makes the numerical modelling of ion beam difficult because of the expected discontinuous nature of the solutions obtained.

Facing the stiffness of the calculations, the requirement on the quality of the results and the calculation time, we focused our efforts on mathematical and numerical developments. In this paper, we propose to develop a moment method and a high order accuracy numerical scheme to solve the Fokker-Planck equation that is sufficiently accurate and fast to be used in operational processes of dose deposition optimization.

2 Physical Modelling

The linear Boltzmann transport equation (LBTE) has been used widely in the study of particle transport for several decades [17]. However, the nature of interaction of the ion is different from that of the neutron: due to the Coulomb interactions, the ion has a large number of small angle scatter interactions. This type of interaction is expressed in nearly singular differential scatter cross sections. It is very unpractical to treat these differential cross sections with conventional means in deterministic methods. To deal with this issue, the Fokker-Planck approximation is used. In this approximation, the small angle scatters and the small energy transfers are described by the Fokker-Planck operators. In this section, we will describe these equations.

2.1 The Boltzmann-Fokker-Planck Equation

We define $f(\mathbf{r}, \epsilon, \mathbf{\Omega}, t)$ as an angular density of ion particles in phase space ($\mathbb{R}^3 \times \mathbb{R}^+ \times \mathbb{S}^2 \times \mathbb{R}^+$). The particle density $N(\mathbf{r}, \epsilon, t)$ can be determined by:

$$N(\mathbf{r}, \epsilon, t) = \int_{\mathbb{S}^2} f(\mathbf{r}, \epsilon', \mathbf{\Omega}', t) d\mathbf{\Omega}' \tag{1}$$

The motion of transported particles in matter is modelled by their fluence $\psi = ||\mathbf{v}|| f(\mathbf{r}, \epsilon, \mathbf{\Omega}, t)$ where $\mathbf{v}$ is the particle speed vector ($||\mathbf{v}|| = \sqrt{2\epsilon/m}$).

The flow of particles through the background medium (target) is described by the LBTE (2):

$$\begin{aligned}\frac{1}{v}\frac{\partial\psi(\mathbf{r},\epsilon,\mathbf{\Omega},t)}{\partial t} &+ \mathbf{\Omega}\cdot\nabla_{\mathbf{r}}\psi(\mathbf{r},\epsilon,\mathbf{\Omega},t) + \sigma_t(\epsilon)\psi(\mathbf{r},\epsilon,\mathbf{\Omega},t)\\ &= \int_{\mathbb{R}^+} d\epsilon' \int_{\mathbb{S}^2} \sigma(\epsilon\to\epsilon',\mathbf{\Omega}\cdot\mathbf{\Omega}')\psi(\mathbf{r},\epsilon',\mathbf{\Omega}',t)d\mathbf{\Omega}'\\ &+ Q(\mathbf{r},\epsilon,\mathbf{\Omega},t),\end{aligned} \tag{2}$$

with $t\in\mathbb{R}^+$ the time, $\epsilon\in\mathbb{R}^+$ the particle energy, $\mathbf{r}\in\mathbb{R}^3$ the position vector, $\mathbf{\Omega}\in\mathbb{R}^3$ the flight direction. $Q(\mathbf{r},\epsilon,\mathbf{\Omega},t)$ is the source term. $\sigma(\epsilon,\to\epsilon',\mathbf{\Omega}\cdot\mathbf{\Omega}')$ is the differential scattering cross section of the ions at the energy ϵ into the direction $\mathbf{\Omega}$. σ_t denotes the total cross section :

$$\sigma_t(\epsilon) = \int_{\mathbb{S}^2}\int_{\epsilon_{min}}^{\epsilon} \sigma(\epsilon\to\epsilon',\mathbf{\Omega}\cdot\mathbf{\Omega}')d\epsilon' d\mathbf{\Omega}'. \tag{3}$$

We define the cross section operator Σ_B, expressed the likelihood of interactions between particles, as stated by

$$\Sigma_B\psi(\mathbf{r},\epsilon,\mathbf{\Omega},t) = \sigma_t(\epsilon)\psi(\mathbf{r},\epsilon,\mathbf{\Omega},t) - \int_0^{\infty}\int_{\mathbb{S}^2} \sigma(\epsilon\to\epsilon',\mathbf{\Omega}\cdot\mathbf{\Omega}')\psi(\mathbf{r},\epsilon',\mathbf{\Omega}',t)d\mathbf{\Omega}'d\epsilon' \tag{4}$$

On the theoretical point of view, the linear Boltzmann collision operator described is appropriate. Although, for numerical considerations, discretizing directly these terms can be difficult. Typically, discretizations of the gain term require the energy grid to be fine enough to capture the peak of Boltzmann cross sections operator Σ_B, which requires a significant number of energy cells.

The time required for slowing down the particles is negligible if compared to the time of irradiation. These assumptions imply that the flux of injected particles can be considered as constant in time and the equation describing the transport of particles is time independent. Instead it is often preferred to substitute the exact integral operator described above by a Fokker-Planck one, reflecting the continuous slowing-down approximation (CSDA) [18]. This approach is based on a hypothesis that a small kinetic energy loss results in a small deviation, the cumulative effect of many soft interactions can be approximated by the continuous energy loss of a charged particle without angular deflection and without production of secondary particles.

With all these assumptions, the fluence of the transported particles satisfies the following equation (called Fokker-Planck equation):

$$\mathbf{\Omega}\cdot\nabla_{\mathbf{r}}\psi(\mathbf{r},\epsilon,\mathbf{\Omega}) + \Sigma_{FP}\psi_n(\mathbf{r},\epsilon,\mathbf{\Omega}) = Q(\mathbf{r},\epsilon,\mathbf{\Omega}) \tag{5}$$

The cross section operator Σ_B can be approximated by the Fokker-Planck (FP) operator Σ_{FP}:

$$\Sigma_{FP}\psi(\mathbf{r},\epsilon,\mathbf{\Omega}) = -\rho\frac{\partial}{\partial\epsilon}(S(\epsilon)\psi(\mathbf{r},\epsilon,\mathbf{\Omega})) - \rho T(\epsilon)\Delta_{\mathbf{\Omega}}\psi(\mathbf{r},\epsilon,\mathbf{\Omega}). \tag{6}$$

with ρ the target weight density ($\mathrm{g.cm}^{-3}$).

We introduce the Laplace–Beltrami operator $\Delta_{\mathbf{\Omega}}\psi$ defined by

$$\Delta_{\mathbf{\Omega}}\psi(\mathbf{r},\epsilon,\mathbf{\Omega}) = \frac{\partial}{\partial\mu}\left((1-\mu^2)\frac{\partial}{\partial\mu}\psi(\mathbf{r},\epsilon,\mathbf{\Omega})\right) + \frac{1}{1-\mu^2}\frac{\partial^2\psi}{\partial\phi^2} \tag{7}$$

and the variables μ and ϕ are the directions of $\mathbf{\Omega}$ in spherical coordinates :

$$(\mu, \sqrt{1-\mu^2}\cos\phi, \sqrt{1-\mu^2}\sin\phi)^T$$

with $\mu = \cos\theta$, θ and ϕ being the polar and azimuthal angles of the vector $\mathbf{\Omega}$, $\mu \in [-1, 1]$, $\phi \in [0, 2\pi]$.

We define the function S the mass stopping power (mass energy loss per unit distance travelled) as:

$$S(\epsilon) = \int_{\epsilon_{min}}^{\epsilon} \int_{\mathbb{S}^2} \epsilon'.\sigma(\epsilon \to \epsilon', \mathbf{\Omega}' \cdot \mathbf{\Omega}) d\mathbf{\Omega}' d\epsilon' \tag{8}$$

and the function T is the momentum transfer cross section, called 'transmission coefficient':

$$T(\epsilon) = \int_{\epsilon_{min}}^{\epsilon} \int_{\mathbb{S}^2} (1 - \mathbf{\Omega}' \cdot \mathbf{\Omega}) \sigma(\epsilon \to \epsilon', \mathbf{\Omega}' \cdot \mathbf{\Omega}) d\mathbf{\Omega}' d\epsilon'. \tag{9}$$

Knowing the mass stopping power, one can estimate the range of an ion beam. The range is defined as the distance travelled by a particle in a medium before all its kinetic energy is lost. If we neglect the small lateral deflections of the ion, for an initial energy E_0 of the ion beam, the range can be calculated by the expression (10):

$$R(E_0) = \int_0^{E_0} \frac{d\epsilon}{\rho S(\epsilon)}. \tag{10}$$

2.2 Transport Coefficients

2.2.1 Stopping Power

The mass stopping power defined by the relation (8) does not provide a practical method for calculating the stopping power.

The theory of energy loss has been developed in many authors, these phenomena were described in many different publications over many decades [19, 20]. When passing through matter, charged particles ionize atoms or molecules along their path. Consequently, these particles gradually lose their energy. The stopping power is the average loss of energy of the particle per unit of distance traveled. The mass stopping power models a property of the material (in MeV.cm^2/g), it is defined by:

$$S(E) = -\frac{1}{\rho}\frac{dE}{dx}, \tag{11}$$

(in this sub-section, E designates the particle energy, in MeV). Since the total energy loss mechanism is divided into two processes (electronic interaction and nuclear interaction), the computation of the SP can be separated into two parts: the electronic stopping power (due to inelastic collisions) and the nuclear stopping power (due to elastic collisions):

$$S(E) = S_e(E) + S_n(E). \tag{12}$$

The electronic stopping power deals with the interaction of the incident ions with the electrons of the target particles. This approximation is possible because the electrons have a much lower mass than the nuclei, the kinetic energy is therefore largely transferred to the electrons. The energy loss by ionization above 500 keV is adequately described by the Bethe-Bloch formula:

$$S_e(E) = \frac{\kappa}{A_P}\frac{Z_T Z_P^2}{\beta^2}\left[\ln\left(\frac{2m_e c^2\beta^2}{< I > (1-\beta^2)}\right) - \beta^2 - \frac{C}{Z_T} - \frac{\delta}{2}\right], \tag{13}$$

with κ the stopping pre-factor (= 0.3071 for stopping units of MeV.cm^2/g), Z_T the target atomic number, Z_P the projectile atomic number, A_P the target atomic weight , $< I >$ the averaged excitation potential per electron. $\frac{C}{Z_T}$ is the 'Shell correction', the density effect term ($\frac{\delta}{2}$) corrects for polarization effects in the target (see Ref. [21]).

The nuclear stopping power is calculated by considering the incident ion and the target nucleus in the center of mass reference frame. The Ziegler's empirical formula [21] which is a modification of the theory of Lindhard *et al.* [22] is used. There have been several extensive theoretical studies of the nuclear stopping power using the rms (root-mean-square) value of the interatomic potential. This is an empirical formula called the universal interatomic potential [21, 23]. This empirical formula is used to evaluate the nuclear stopping power of an ion in a solid. The accuracy of the empirical fit was less than 1%. In reduced units, the nuclear stopping power is given by:

$$S_n(E) = \frac{8.462 \times 10^{-15} Z_P Z_T M_P S_n^u(\varepsilon)}{(M_P + M_T)(Z_P^{0.23} + Z_T^{0.23})} \quad (\text{eV.cm}^2/\text{atom}). \tag{14}$$

ε is the reduced energy in units of keV/nucleon:

$$\varepsilon = \frac{32.53 M_T E}{Z_P Z_T (M_P + M_T)(Z_P^{0.23} + Z_T^{0.23})} \tag{15}$$

with M_P, M_T the atomic masses of projectile and target respectively.
$S_n^u(\varepsilon)$ is the reduced nuclear stopping power (16) :

$$\begin{cases} S_n^u(\varepsilon) = \dfrac{\ln(1. + 1.1383\varepsilon)}{2[\varepsilon + 0.01321\varepsilon^{0.21226} + 0.19593\varepsilon^{0.5}]} & \text{for } \varepsilon \leq 30 \\ S_n^u(\varepsilon) = \dfrac{\ln(\varepsilon)}{2\varepsilon} & \text{for } \varepsilon > 30 \end{cases} \tag{16}$$

2.2.2 Stopping power of a compound material

The stopping power of a compound can be expressed as a combination of the stopping power of the constituent elements as a convex combination:

$$S(E) = \sum_k Y_k S_k(E) \tag{17}$$

where Y_k is the weight fraction of element k and such that $\sum_k Y_k = 1$.

Figure (1) shows the stopping powers of Protons and Alpha in water estimated by relations (12-17) in comparison with [24].

Knowing $S(E)$, we integrate the relation (18) using the 4th order Runge-Kutta scheme to obtain the ion energy all along the path from the initial energy (E_0):

$$\frac{dE}{dx} = -\rho S(E) \tag{18}$$

This integration provides us the value of the range when the charged particle energy is all deposited ($E = 0$) (see Figure 2).

2.2.3 Momentum transfer cross section

The momentum transfer cross section is necessary to describe the angular diffusion due to elastic collisions. From the relation (9), $T(E)$ can be expressed:

$$T(E) = \int_0^{2\pi} \int_{-\pi}^{\pi} \sigma(E, \cos\theta)(1 - \cos\theta) \sin\theta d\theta d\phi. \tag{19}$$

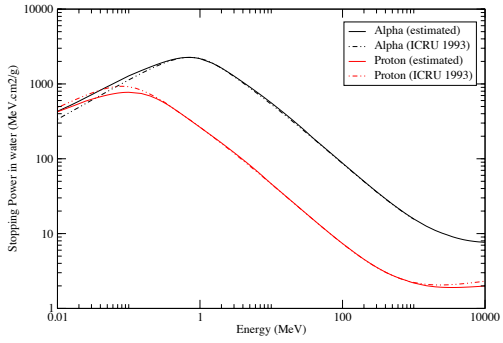

Figure 1: Stopping power of Protons (H^+) and Alpha (He^+) in water - Comparison between our estimation and [24].

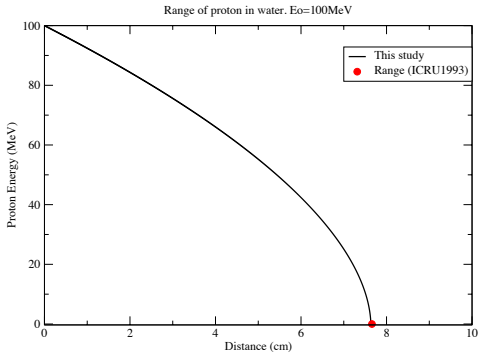

Figure 2: Energy path of protons in water for an initial energy $E_0 = 100$ MeV - a beam ion, coming in the target with an initiale energy E_0, deposits there all its energy until becoming still.

Using the Rutherford differential cross section [25],

$$\sigma(E, \cos\theta) = \frac{d\sigma}{d\Omega} = \left(\frac{Z_P Z_T e^2}{4E}\right)^2 \frac{1}{\sin^4(\theta/2)}, \tag{20}$$

(where e is the elementary electric charge), one obtain:

$$T(E) = 2\pi \left(\frac{Z_P Z_T e^2}{E}\right)^2 \left[\ln(2\sin^2(\theta/2)\right]_{\theta_0}^{\pi} \tag{21}$$

A typical feature of the relation (21) is that it increases very rapidly for small angles and even becomes ∞ at $\theta \to 0$; small-angle scattering corresponds to very large impact parameters. A cutoff in the smallest possible scattering angle θ_0 must be imposed from physical considerations.

The resolution of such a system is complex in terms of software development and calculation time. We detail in the next section the moment method used that allows to reduce the number of degrees of freedom.

3 Moment Method : M_1 Model

An angular moment model for the Fokker-Planck equation was proposed by Dubroca *et al.* [14]. Its ability to simulate efficiently the transport of energetic particles has been demonstrated in the context of photon- and radio- therapy [16]. Therefore, we will use theses studies to develop our methods for ion beams.

3.1 Definitions

The $i-$th angular moment of the function ψ is defined by :

$$\psi^i(\mathbf{r},\epsilon) = \int_{\mathbb{S}^2} \underbrace{\mathbf{\Omega}\otimes ... \otimes \mathbf{\Omega}}_{i \text{ times}} .\psi(\mathbf{r},\epsilon,\mathbf{\Omega})d\mathbf{\Omega}. \tag{22}$$

The three firsts moments are written:

$$\begin{aligned}
\psi^0(\mathbf{r},\epsilon) &= \int_{\mathbb{S}^2} \psi(\mathbf{r},\epsilon,\mathbf{\Omega})d\mathbf{\Omega} = \langle\psi\rangle,\\
\boldsymbol{\psi^1}(\mathbf{r},\epsilon) &= \int_{\mathbb{S}^2} \mathbf{\Omega}\psi(\mathbf{r},\epsilon,\mathbf{\Omega})d\mathbf{\Omega} = \langle\mathbf{\Omega}\psi\rangle,\\
\boldsymbol{\psi^2}(\mathbf{r},\epsilon) &= \int_{\mathbb{S}^2} \mathbf{\Omega}\otimes\mathbf{\Omega}.\psi(\mathbf{r},\epsilon,\mathbf{\Omega})d\mathbf{\Omega} = \langle\mathbf{\Omega}\otimes\mathbf{\Omega}\psi\rangle.
\end{aligned} \tag{23}$$

Using the definitions of the angular moments (23), one notices that ψ^0 is non negative as the integral of a non-negative fluence function. It is also clear that $||\boldsymbol{\psi^1}|| \leq \psi^0$.

Proposition 1. *Positivity of ψ^0 : $\psi^0 \geq 0$.*

Proposition 2. *Flux limitation: $\|\boldsymbol{\psi^1}\| \leq \psi^0$.*

These properties lead to the following definition of the realizability domain $\mathcal{A}$.

Definition 1. $\mathcal{A} = \left\{(\psi^0,\boldsymbol{\psi^1}) \in \mathbb{R}\times\mathbb{R}^3,\ \psi^0 \geq 0,\ ||\boldsymbol{\psi^1}|| \leq \psi^0\right\}.$

This condition can be interpreted at the physical level by the boundedness of the fluxes.

Proposition 3. *The realizability domain $\mathcal{A}$ is a convex cone i.e.*

- *If $u \in \mathcal{A}$ then $\forall\alpha \in \mathbb{R}^+,\ \alpha u \in \mathcal{A}$;*
- *If $(u,\ v) \in \mathcal{A}\times\mathcal{A}$ then $\forall\alpha \in [0,1],\ \alpha u + (1-\alpha)v \in \mathcal{A}$;*
- *Consequence of these two properties:*
  If $(u,\ v) \in \mathcal{A}\times\mathcal{A}$ then $\forall(\alpha,\ \beta) \in \mathbb{R}^+\times\mathbb{R}^+,\ \alpha u + \beta v \in \mathcal{A}$.

This property will be used when constructing numerical schemes for moment equations in order to prove that such schemes preserve the realizability property from one step to another.

3.2 System of moment equations

By averaging the equation (5) and the multiplication by $\mathbf{\Omega}$ of this equation over $\mathbf{\Omega}$ we obtain the system of moment equations:

$$\begin{cases} \nabla_{\mathbf{r}}.\boldsymbol{\psi^1}(\mathbf{r},\epsilon) = \dfrac{\partial}{\partial\epsilon}\left(\rho S(\epsilon)\psi^0(\mathbf{r},\epsilon)\right) + Q^0(\mathbf{r},\epsilon) \\ \nabla_{\mathbf{r}}.\boldsymbol{\psi^2}(\mathbf{r},\epsilon) = \dfrac{\partial}{\partial\epsilon}\left[\rho S(\epsilon)\boldsymbol{\psi^1}(\mathbf{r},\epsilon)\right] - 2\rho T(\epsilon)\boldsymbol{\psi^1}(\mathbf{r},\epsilon) + \boldsymbol{Q^1}(\mathbf{r},\epsilon) \end{cases} \tag{24}$$

The system (24) can be re-written in the vectorial form

$$\rho(\mathbf{r})\frac{\partial S(\epsilon)\mathbf{U}}{\partial\epsilon} - \nabla_{\mathbf{r}}.\mathcal{F}(\mathbf{U}) = \mathcal{T}.\mathbf{U} + \mathbf{Q} \tag{25}$$

In semi-developed form:

$$\rho(\mathbf{r})\frac{\partial S(\epsilon)\mathbf{U}}{\partial\epsilon} - \frac{\partial\mathcal{F}_x(\mathbf{U})}{\partial x} - \frac{\partial\mathcal{F}_y(\mathbf{U})}{\partial y} - \frac{\partial\mathcal{F}_z(\mathbf{U})}{\partial z} = \mathcal{T}.\mathbf{U} + \mathbf{Q} \tag{26}$$

$$\mathbf{U} = \begin{pmatrix} \psi^0 \\ \psi^1_x \\ \psi^1_y \\ \psi^1_z \end{pmatrix}, \quad \mathcal{T} = 2\rho(\mathbf{r})T(\epsilon)\begin{pmatrix} 0 & 0 & 0 & 0 \\ 0 & 1 & 0 & 0 \\ 0 & 0 & 1 & 0 \\ 0 & 0 & 0 & 1 \end{pmatrix},$$

$$\mathcal{F}_x(\mathbf{U}) = \begin{pmatrix} \psi^1_x \\ \psi^2_{xx} \\ \psi^2_{yx} \\ \psi^2_{zx} \end{pmatrix}, \quad \mathcal{F}_y(\mathbf{U}) = \begin{pmatrix} \psi^1_y \\ \psi^2_{xy} \\ \psi^2_{yy} \\ \psi^2_{zy} \end{pmatrix}, \quad \mathcal{F}_z(\mathbf{U}) = \begin{pmatrix} \psi^1_z \\ \psi^2_{xz} \\ \psi^2_{yz} \\ \psi^2_{zz} \end{pmatrix}.$$

However, this system doesn't admit a unique solution. A central issue in the definition of the moment model is the choice of the closure, which writes the highest moment as a function of the lower ones.

3.3 Entropic Closure

A minimum entropy approach to the closure problem was applied by Levermore [11].

We want that our model applied to a closed and isolated system evolves to equilibrium, the same way that the original Fokker-Planck equation moves to more probable states, due to the collisions between particles. The second law of thermodynamics asserts that the entropy attains its minimum, as the system reaches the state of equilibrium. The angular entropy of our system of moment equations is defined as:

$$\mathcal{H}(\psi) = \int_{S^2} (\psi\ln\psi - \psi)\, d\mathbf{\Omega}. \tag{27}$$

We use the entropy minimization principle (Boltzmann H-Theorem [26]) to close the moment equation system, the second order moment $\boldsymbol{\psi^2}$ will be expressed as a function of ψ^0 and $\boldsymbol{\psi^1}$. The underlying fluence function ψ is obtained as a solution of the following minimisation problem:

$$\min\left\{\mathcal{H}(\psi)/\forall\epsilon\in\mathbb{R}^+, \int_{\mathbb{S}^2}\psi\left(\mathbf{r},\epsilon,\mathbf{\Omega}\right)d\mathbf{\Omega} = \psi^0(\mathbf{r},\epsilon), \int_{\mathbb{S}^2}\mathbf{\Omega}\psi(\mathbf{r},\epsilon,\mathbf{\Omega})d\mathbf{\Omega} = \boldsymbol{\psi^1}(\mathbf{r},\epsilon)\right\}. \tag{28}$$

(28) admits a solution [14]:

$$\psi(\epsilon, \mathbf{r}) = \exp(\lambda_0(\epsilon, \mathbf{r}) + \boldsymbol{\lambda_1}(\epsilon, \mathbf{r}).\boldsymbol{\Omega}) \tag{29}$$

with $(\lambda_0, \boldsymbol{\lambda_1}) \in \mathbb{R} \times \mathbb{R}^3$.
We define the anisotropy factor α as $\mid \alpha \mid = \frac{\|\boldsymbol{\psi^1}\|}{\psi^0}$, bounded in the interval [0, 1].

By using the Maxwell-Boltzmann-type distribution that assures the positivity of particle density, $\boldsymbol{\psi^2}$ can be computed [14]:

$$\boldsymbol{\psi^2} = \psi^0 \left(\frac{1-\chi}{2}\mathbb{I} + \frac{3\chi - 1}{2} \frac{\boldsymbol{\psi^1} \otimes \boldsymbol{\psi^1}}{\| \boldsymbol{\psi^1} \|^2} \right), \tag{30}$$

where $\mathbb{I}$ is the identity tensor, the Eddington factor χ can be related to the anisotropy factor α under interpolated form:

$$\chi(\alpha) \simeq \frac{1}{3}(1 + \alpha^2 + \alpha^4) \tag{31}$$

Remark 1. *For $\alpha = 0$, we have $\chi = \frac{1}{3}$, which corresponds to the P_1 model, largely used in the context of radiative transfer.*

3.4 Dose

The principle of dose calculation is to solve the above equations for ion transport and then to use the calculated fluence to determine the absorbed dose. The dose can be calculated from the stopping power :

$$D(\mathbf{r}) = \int_0^\infty S(\epsilon)\psi^0(\mathbf{r}, \epsilon)d\epsilon \tag{32}$$

4 Numerical Methods

The spatial domain $\mathcal{D}$ is discretized using a uniform cartesian grid. We assume that the source term Q does not exist.

4.1 Energetic Derivate: Explicit Method

Using an energy explicit Euler scheme and integrating in energy retrogradeNote ($\epsilon_{\max} \rightarrow \epsilon_{\min}$), the 3D equation system over a control volume $[x_{i-1/2}, x_{i+1/2}] \times [y_{j-1/2}, y_{j+1/2}] \times [z_{k-1/2}, z_{k+1/2}]$ can be written under the discretized form:

$$(\rho_{i,j,k} S^n \mathbb{I} + \Delta\epsilon.\mathcal{T}^n)\mathbf{U}^n_{i,j,k} = \rho_{i,j,k} S^{n+1} \mathbf{U}^{n+1}_{i,j,k} - \sum_{l=i,j,k} \frac{\Delta\epsilon}{\Delta x_l} (\mathcal{F}^{n+1}_{l+1/2} - \mathcal{F}^{n+1}_{l-1/2}) \tag{33}$$

$l = i, \Delta x_i = \Delta x$, $\mathcal{F}_{i+1/2}$ corresponds to the x direction discretized flux $\mathcal{F}_x(x_{i+1/2})$;
$l = j, \Delta x_j = \Delta y$, $\mathcal{F}_{j+1/2}$ corresponds to the y direction discretized flux $\mathcal{F}_y(y_{j+1/2})$;
$l = k, \Delta x_k = \Delta z$, $\mathcal{F}_{k+1/2}$ corresponds to the z direction discretized flux $\mathcal{F}_z(z_{k+1/2})$.

Thereafter, we will note $\mathcal{S}^n_{i,j,k} = (\rho_{i,j,k} S^n \mathbb{I} + \Delta\epsilon.\mathcal{T}^n_{i,j,k})$.

Using an explicit scheme, one must pick the energy step according to the Courant-Friedrish-Levy (CFL) condition. This condition will be discussed as well as the spatial numerical scheme in the subsection 4.2.1. An implicit scheme has been experimented but was suffering a large amount of numerical diffusion in comparison with the explicit method. Since we are looking for highly accurate solutions, we will only mention the explicit approach in this paper.

4.2 Spatial Resolution

For sake of simplicity, we only focus on the discretization of the $1D_x$ equation system. The extension to higher dimensions is straightforward on a cartesian grid. The realizability of standard high-order finite-volume schemes in space is discussed. We will notice an approximation of $\mathbf{U}_i^n = \mathbf{U}(x_i, \epsilon^n)$ at the position x_i and the energy ϵ^n.

4.2.1 First Order Approximation: HLL Scheme

The spatial discretization is achieved with a standard finite volume scheme using the Harten-Lax-van Leer (HLL) [27] approximate Riemann solver to compute the fluxes at the cell interfaces in the x direction. This numerical scheme is commonly used for the moment equations due to its capability to preserve the realizability from one energy step to another, it is positively conservative if the absolute value of the maximal and minimal wavespeeds satisfies certain stability bounds.

The HLL scheme [27] solves the Riemann problem approximately by assuming a single state between the left and right states:

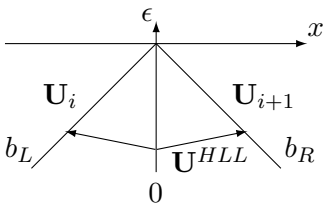

$$\widetilde{\mathbf{U}}(x/\epsilon) = \begin{cases} \mathbf{U}_i & \text{if } x/\epsilon < b^L \\ \mathbf{U}_i^{\mathrm{HLL}} & \text{if } b^L < x/\epsilon < b^R \\ \mathbf{U}_{i+1} & \text{if } x/\epsilon > b^R \end{cases} \quad (34)$$

where b^L and b^R are the smallest and the largest wave velocities at the interface $x_{i+1/2}$, they correspond to the eigenvalues of the Jacobian matrix associated to the flux function $\mathcal{F}(\mathbf{U})$.

Using an energy explicit Euler scheme and integrating the 1D equation system on a control volume $(x_{i-1/2},\ x_{i+1/2})$, we obtain:

$$\rho_i \frac{S(\epsilon^{n+1})\mathbf{U}_i^{n+1} - S(\epsilon^n)\mathbf{U}_i^n}{\Delta\epsilon} - \frac{F_{i+1/2}^{\mathrm{HLL}} - F_{i-1/2}^{\mathrm{HLL}}}{\Delta x} = \mathcal{T}_i^n \mathbf{U}_i^n \quad (35)$$

where the flux function $F_{i+1/2}^{\mathrm{HLL}}$ is defined as:

$$F_{i+1/2}^{\mathrm{HLL}} = \frac{b^+\mathcal{F}_i - b^-\mathcal{F}_{i+1} + b^+b^-(\mathbf{U}_{i+1} - \mathbf{U}_i)}{b^+ - b^-} \quad (36)$$

with $b^+ = \max(b^R, 0)$, and $b^- = \min(b^L, 0)$.

For the particular case, $b^+ = 1$ and $b^- = -1$, the flux function $\mathcal{F}_{i+1/2}$ is written:

$$\begin{aligned} F_{i+1/2} &= F(\mathbf{U}_i, \mathbf{U}_{i+1}) \\ F_{i+1/2} &= \frac{1}{2}(\mathcal{F}_i + \mathcal{F}_{i+1} - (\mathbf{U}_{i+1} - \mathbf{U}_i)) \end{aligned} \quad (37)$$

Finally, by integrating in energy degeneration, the state at ϵ^n can be obtained:

$$\mathcal{S}_i^n \mathbf{U}_i^n = \mathbf{U}_i^{n+1}(\rho_i S^{n+1} - \frac{\Delta\epsilon}{\Delta x}) + \frac{\Delta\epsilon}{2\Delta x}(\mathbf{U}_{i+1}^{n+1} - \mathcal{F}(\mathbf{U}_{i+1}^{n+1})) + \frac{\Delta\epsilon}{2\Delta x}(\mathbf{U}_{i-1}^{n+1} + \mathcal{F}(\mathbf{U}_{i-1}^{n+1})) \quad (38)$$

CFL Condition:

This scheme (38) is stable under CFL condition:

$$CFL = \frac{\Delta\epsilon}{\rho_{\min} S^{n+1} \Delta x} < 1, \quad (39)$$

with $\rho_{\min} = \min(\rho_i, \forall\ i \in \mathcal{D})$.

The size of the energy step $\Delta\epsilon$ is chosen according to this condition. It becomes very restrictive when the density ρ of the target is low (for example $\rho_{Air} = 1.204\ 10^{-3}\text{g.cm}^{-3}$).

4.2.2 Realizability

In order to provide deeper physical meaning to the solution of moment equation, one aims to relate the solution ψ^k of moment equation such as (24) to an underlying kinetic fluence ψ, numerical schemes applied to the system (26) need to preserve the realizability property.

Lemma 1. *If* $\mathbf{U} \in \mathcal{A}$ *then* $\mathbf{U} \pm \mathcal{F}(\mathbf{U}) \in \mathcal{A}$.

Proof. According to Definition 1:

$\exists \psi \geq 0,\ \forall \mathbf{U} \in \mathcal{A}$ such as

$$\mathbf{U} \pm \mathcal{F}(\mathbf{U}) = \left\langle \psi \begin{pmatrix} 1 \\ \mu \end{pmatrix} \right\rangle \pm \left\langle \psi \begin{pmatrix} \mu \\ \mu^2 \end{pmatrix} \right\rangle = \left\langle (1 \pm \mu)\psi \begin{pmatrix} 1 \\ \mu \end{pmatrix} \right\rangle$$

As $\mu \in [-1, 1]$ then $\mathbf{U} \pm \mathcal{F}(\mathbf{U}) \in \mathcal{A}$. □

Using this property, we can show that out method preserves the realizability property from an energy step to the next one:

Proposition 4. *If we assume the CFL condition (*$\frac{\Delta\epsilon}{\rho S \Delta x} < 1$*) then for* $\mathbf{U}_i^{n+1} \in \mathcal{A}$ *, the scheme (38) provides* $\mathbf{U}_i^n \in \mathcal{A}$ *.*

Proof. From the equation (38), we examine term by term

$$\mathcal{S}_i^n.\mathbf{U}_i^n = \underbrace{\mathbf{U}_i^{n+1}(\rho_i S^{n+1} - \frac{\Delta\epsilon}{\Delta x})}_{\in \mathcal{A} \text{ if } \frac{\Delta\epsilon}{\rho S \Delta x} < 1} + \frac{\Delta\epsilon}{2\Delta x} \underbrace{(\mathbf{U}_{i+1}^{n+1} - \mathcal{F}(\mathbf{U}_i^{n+1}))}_{\in \mathcal{A} \text{ see Lemma 1}} + \frac{\Delta\epsilon}{2\Delta x} \underbrace{(\mathbf{U}_{i-1}^{n+1} + \mathcal{F}(\mathbf{U}_{i-1}^{n+1}))}_{\in \mathcal{A} \text{ see Lemma 1}}.$$

If the CFL restriction is satisfied, the updated state is a positive combination of realizable states, it is therefore realizable according to Proposition 3. □

4.2.3 High Order scheme: Second order approximation

The most widely used second-order finite volume scheme is the Monotonic Upstream-centered Scheme for Conservation Laws (MUSCL) scheme (see Ref. [19]). We use Van Leer's techniques to extrapolate the face centered pointwise values of the conservative variables $\mathbf{U}_i^n$ in each cell from the initial volume averaged data. The principle is to start from the definite piecewise constant solution, then to evaluate the slopes and to reconstruct a piecewise affine solution in the x direction.

We then use theses high precision states to solve the Riemann problem and obtain high order estimations of the fluxes.

The slope limiter plays an essential role in suppressing spurious numerical oscillations.

$$\widetilde{\mathbf{U}}_i(x) = \mathbf{U}_i + \frac{x - x_i}{\Delta x}\boldsymbol{\eta_i} \tag{40}$$

where $\boldsymbol{\eta_i}$ denotes the slope of the linear function on the cell $(x_{i-1/2},\ x_{i+1/2})$.

We consider the inner approximations in the cell i (see Figure 3), located at $x = x_{i-1/2}$ and $x = x_{i+1/2}$. These approximations are denoted $\widetilde{\mathbf{U}}_i^{\pm}$ and are defined by

$$\widetilde{\mathbf{U}}_i^{\pm} = \mathbf{U}_i(x_{i\pm1/2}) = \mathbf{U}_i + \Delta\mathbf{U}_i^{\pm} \tag{41}$$

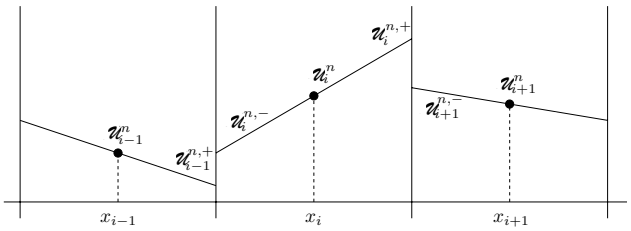

Figure 3: Variation

where the increment $\Delta \mathbf{U}_i^{\pm}$ is defined by :

$$\Delta \mathbf{U}_i^{\pm} = \pm \frac{1}{2} \boldsymbol{\eta_i} \tag{42}$$

The space second order scheme is written:

$$\mathcal{S}_i^n \mathbf{U}_i^n = \rho . S_i^n \mathbf{U}_i^{n+1} - \frac{\Delta \epsilon}{\Delta x} (F(\mathbf{U}_i^+, \mathbf{U}_{i+1}^-) - F(\mathbf{U}_{i-1}^+, \mathbf{U}_i^-)) \tag{43}$$

The main difficulty lies in the construction of the vector increment $\Delta \mathbf{U}_i^{\pm}$.
Several choices for the slope $\boldsymbol{\eta_i}$ are proposed [28, 29]. In this paper, we can use

$$\begin{array}{ll} & \boldsymbol{\eta_i} = \text{minmod}\left(\mathbf{U}_i - \mathbf{U}_{i-1}, \mathbf{U}_{i+1} - \mathbf{U}_i\right), \\ \text{or} & \boldsymbol{\eta_i} = \text{superbee}\left(2(\mathbf{U}_i - \mathbf{U}_{i-1}), 2(\mathbf{U}_{i+1} - \mathbf{U}_i), \mathbf{U}_{i+1} - \mathbf{U}_{i-1}\right). \end{array} \tag{44}$$

With the minmod function defined by

$$\forall (x,y) \in \mathbb{R}^2, \ \text{minmod}\,(x,y) = \begin{cases} 0 & \text{if } xy \leq 0 \\ x & \text{if } |x| \leq |y| \\ y & \text{else} \end{cases} . \tag{45}$$

and the superbee limiter:

$$\text{superbee}\,(x,y,z) = \text{minmod}\,(x,y,z) \tag{46}$$

with

$$\forall (x,y,z) \in \mathbb{R}^3, \ \text{minmod}\,(x,y,z) = \max(0, \min(x,y,z)) + \min(0, \max(x,y,z)). \tag{47}$$

In order to ensure that the scheme preserves the realizability of the solution, we use the slope limitation procedure proposed by Berthon [30].

We introduce now a parameter δ :

$$\widetilde{\mathbf{U}}_i^{\pm} = \mathbf{U}_i \pm \delta_i \Delta \mathbf{U}_i^{\pm} \quad \text{such as } \widetilde{\mathbf{U}}_i^{\pm} \in \mathcal{A} \tag{48}$$

Then

$$\begin{cases} \psi^0 \pm \delta_i \Delta \mathbf{U}_i^{0\pm} \geq 0 & \text{(see Proposition 1)} \\ |\psi^1 \pm \delta_i \Delta \mathbf{U}_i^{1\pm}| \leq \psi^0 \pm \delta_i \Delta \mathbf{U}_i^{0\pm} & \text{(see Proposition 2)} \end{cases} \tag{49}$$

The system (49) admits 4 solutions :

$$\delta_i^{1,2,3,4} = \frac{\left(\mp(\Delta \mathbf{U}_i^{0\pm} \psi_i^0 - \Delta \mathbf{U}_i^{1\pm} \psi_i^1) \pm \sqrt{\Delta}\right)}{(\Delta \mathbf{U}_i^{0\pm})^2 - (\Delta \mathbf{U}_i^{1\pm})^2} \tag{50}$$

with $\Delta = (\Delta\mathbf{U}_i^{0\pm}\psi_i^0 - \Delta\mathbf{U}_i^{1\pm}\psi_i^1)^2 - ((\Delta\mathbf{U}_i^{0\pm})^2 - (\Delta\mathbf{U}_i^{1\pm})^2)((\psi_i^0)^2 - (\psi_i^1)^2)$.

Finally, the following nonlinear realizability condition is determined:

$$\delta_i = \min(1,\ \delta_i^*) \quad \text{with } \delta_i^* = \min(\delta_i^j \ \text{ if } \delta_i^j > 0, j = 1..4) \tag{51}$$

CFL Condition:

Theorem 1. *[31]: If the first order scheme (33) is realizable under CFL condition ($CFL < 1$) then the second order scheme (43-51) is realizable under CFL condition $\frac{1}{2}$ ($CFL < \frac{1}{2}$) .*

4.2.4 High Order scheme: Fourth order approximation

We turn now to a higher order approximation using a fourth order MUSCL TVD scheme [32].

$$\mathbf{U}_i^{\pm} = \mathbf{U}_i + \delta_i(\Delta u)_i^{\pm} \tag{52}$$

Similar to the second order scheme, the fourth order scheme proceeds in 2 steps. At the first step, we construct the vector increment $(\Delta u)_i^{\pm}$, and at the second, we determine the slope limitation δ_i. This δ_i will be calculated in the same way as the second order scheme (see eq. 48 - 51). Although, we have to redefine the increments $(\Delta u)_i^{\pm}$.

The fourth order MUSCL reconstruction reads :

$$\begin{aligned}
(\Delta u)_i^- &= -\frac{1}{6}\left(2\Delta^*\bar{u}_{i-1/2} + \Delta^*\tilde{u}_{i+1/2}\right), \\
(\Delta u)_i^+ &= \frac{1}{6}\left(\Delta^*\bar{u}_{i-1/2} + 2\Delta^*\tilde{u}_{i+1/2}\right),
\end{aligned} \tag{53}$$

where

$$\begin{aligned}
\Delta^*\bar{u}_i &= \text{minmod}\left(2\Delta^* u_{i-1/2}, 4\Delta^* u_{i+1/2}\right), \\
\Delta^*\tilde{u}_i &= \text{minmod}\left(2\Delta^* u_{i+1/2}, 4\Delta^* u_{i-1/2}\right),
\end{aligned} \tag{54}$$

and

$$\begin{aligned}
\Delta^* u_{i+1/2} &= \Delta u_{i+1/2} - \frac{1}{6}\Delta^3\bar{u}_{i+1/2}, \\
\Delta^3\bar{u}_{i+1/2} &= \Delta u^a_{i-1/2} - 2\Delta u^b_{i+1/2} + \Delta u^c_{i+3/2},
\end{aligned}$$

with

$$\begin{aligned}
\Delta u^a_{i-1/2} &= \text{minmod}\left(\Delta u_{i-1/2}, 2\Delta u_{i+1/2}, 2\Delta u_{i+3/2}\right), \\
\Delta u^b_{i+1/2} &= \text{minmod}\left(\Delta u_{i+1/2}, 2\Delta u_{i-1/2}, 2\Delta u_{i+3/2}\right), \\
\Delta u^b_{i+3/2} &= \text{minmod}\left(\Delta u_{i+3/2}, 2\Delta u_{i-1/2}, 2\Delta u_{i+1/2}\right).
\end{aligned}$$

Our method is thus fully described. It was parallelized in Open-MP frame. In the following section, one presents some benchmarks.

Target	Density (g.cm^{-3})	Composition (weight fraction)
Al	2.7	Al 1
Bone	1.85	H 0.034000, C 0.155000, N 0.042000, O 0.435000, Na 0.001000, Mg 0.002000, P 0.103000, S 0.003000, Ca 0.225000
Lung	0.26	H 0.103000, C 0.105000, N 0.031000, O 0.749000, Na 0.002000, P 0.002000, S 0.003000, Cl 0.003000, K 0.002000
Water	1.0	H 0.1111, O 0.8889

Table 1: Characteristics of considered material target

5 Numerical Results and Discussions

5.1 1D Validations : Bragg Curve

The Bragg curve is characteristic to heavy charged particles and describes the energy loss of ionizing radiation during its path through matter. This peak occurs because the effective cross-section increases immediately before the particle stops. For most of the ion path, the charge remains unchanged and the specific energy loss increases as a function of $1/v^2$. Towards the end of the course, the charge is changed by capturing electrons and the curve abruptly decreases.

Uni-dimensional simulations of mono-energetic proton beam are performed with 250 cells in the x direction, the Bragg peak is obtained with accuracy (Figure 4) for 5.10^{-2} seconde CPU, above 30 minutes with Monte Carlo GEANT4 code [33]. The first order scheme provides a good result at the beginning of the path but suffers from an important amount of numerical diffusion that prevents it to correctly capture the Bragg peak. The minmod second order scheme is not sufficient sharp. For the same number of cells, the peak captured by the 4th order scheme is much higher. Excellent results are obtained with the superbee 2nd order scheme (see Figure 4).

It appears that developping a 4th order scheme is necessary to obtain an accurate simulation of the ion beam propagation. Indeed, the superbee 2nd order and the 4th order schemes require noticeably the same CFL number (rather 0.1-0.2 in practice), smaller than the minmod 2nd order CFL. But we can use a smaller amount of cells with the 4th order scheme. This allows to have a more affordable computation complexity for multi-dimensional simulations.

Otherwise, one can notice that for an equivalent initial energy E_0, the Alpha range is 10 times smaller than the Proton one. The phenomenon is not linearly proportional to the molar mass of the projectile.

These results allow us to validate our approach physical model and numerical code.

5.2 1D Simulations : Presence of a single insert

We consider the following geometry (Figure 5). Within 10 cm of water length, a different material is placed from 2 to 4 cm. Four cases are considered : Water (homogeneous medium), Aluminum, Bone and Lung. Their composition is on the Table (1). In this part, we are interested in the simulation of the Proton beam propagation of initial energy ($E_0 = 100$ MeV).

Figure (6) regroups numerical results of 4 cases. This figure highlights the influence of the weight density of target on the range of the dose deposition. The lung is lighter than the water, thus the peak is located further away from the source, unlike the cases of aluminum and bone. The 2nd and 4th order schemes are used with 500 cell mesh. The Bragg peak heights obtained with the 4th order

scheme are more important. The numerical dissipation is minimized with this scheme. The range of each case is compared with the result obtained by the theory (Eq. 18). The agreement between two approaches is excellent (Figure 7).

5.3 2D Alpha beam in Non-homogeneous Medium

We consider a test-case corresponding to the physical setup represented in Figure (8). The calculation domain is by a 10×5 cm^2. The main material is water; at $x = 2$ cm, a 1 cm layer of Aluminum adjacent to a 2 cm layer of bone is placed. The Alpha beam from the left dimension is 1 cm wide, centered at $y = 2.5$ cm, for $E_0 = 480$ MeV. We use a cartesian 500×250 mesh for this case. The simulation is realized using the 4th order scheme in 811 secondes CPU with 2.6 GHz 6 Core i7 Intel Processor.

The lateral straggling of the beam is very low because of the ion mass. One observes a lateral expansion of the dose at the end of the path (Figure 9). Thus, we can expect to find the Bragg curve all along the beam axis ($y = 2.5$ cm). In Figure (10), the dose axial distribution is presented and compared with the 1D curve. The theoretical energy path (Eq. 18) is also plotted. The lateral diffusion leads to a small weak shortcut of the range and a lower peak intensity, but the overall behaviour of Bragg curve is very well reproduced.

5.4 2D Proton beam in presence of a half width air insert

We now want to test our method's ability to deal with important density gradient, for instance, liquid and air ($\rho = 1.0$ g.cm^{-3}) and air ($\rho = 1.204\ 10^{-3}$g.cm^{-3}). This test-case was proposed in [34]. A conventional analytical pencil beam algorithm and a Monte Carlo particle simulation are realized by [34]. The benchmark consists in considering a 150×80 mm^2 calculation domain. A 128 MeV Proton beam is coming in water from the left, centered at $y = 40$ mm with 10 mm wide. In the domain, an air pocket is present from $x = 50$ to 70 mm, $y = 40$ to 80 mm. The time steps are very small because of the low density of the air (see paragraph 4.2.1 for discussions), the time calculation is important for 150×80 mesh (3650 secondes CPU with the minmod 2nd order scheme).

The pencil beam method is commonly used for dose calculations in intensity- modulated radiation therapy (IMRT) [35]. While PB algorithm is very fast, the limitations of PB algorithms in heterogeneous media are well known. This is due to the fact that PB algorithms use a one-dimensional density correction which does not accurately model the accurately model the distribution of secondary electrons in media of different densities. Figure (11) shows the spatial distribution of the dose. As in the Alpha beam case, the lateral diffusion is not important, until 60 mm. Some of charged particles crossed through the air zone deposited their energy away from the source. The moments method quantitatively reproduces the behavior of ion propagation in this medium.

5.5 3D Simulation

For this case, the 100 MeV Proton $d_0 = 1$ cm diameter beam is coming from the left in the water. It is centered at ($y_0 = 3.5$ cm, $z_0 = 3.5$ cm) at its direction is inclined by ($\theta = -5^o,\ \phi = 30^o$). The boundary condition of ψ^0, and $\boldsymbol{\psi^1}$ at the beam is determined by:

$$\forall x = 0,\ \begin{cases} \psi^0,\ \boldsymbol{\psi^1} = \psi^0 \begin{pmatrix} \cos\theta \\ \sin\theta\cos\phi \\ \sin\theta\sin\phi \end{pmatrix} & \text{for } \sqrt{(y-y_0)^2 + (z-z_0)^2} \leq \dfrac{d_0}{2} \\ \psi^0 = 0,\ \boldsymbol{\psi^1} = \mathbf{0} \text{ else} \end{cases} . \tag{55}$$

A ($200 \times 120 \times 120$) cartesian mesh is used for ($10 \times 6 \times 6\text{cm}^3$) calculation domain. Bone rectangular parallelepipeds (of $10 \times 10\text{mm}^2$ section and of $10 \times 5\text{mm}^2$ section, 60 mm length) are placed in parallel in the z direction. A Lung ($2 \times 3 \times 3\text{cm}^3$) rectangular parallelepiped is located at ($x \in [4, 6]$, $y \in [0, 3]$, $z \in [1.5, 4.5]$) (see Figure 12 (a) and (b)). This case requires 5 hours of calculation time in 4th order accuracy.

Figure (13) shows how the beam propagates in the medium: some of charged particles only pass through water medium, some also pass through the bone, a small part meet three materials along their path.

Figure (14) shows the complexity due to the interaction of the different characteristics of this beam. The ions that have passed through the three materials deposit their remaining energy farthest as predicted in the subsection (5.2) for the case with a lung insert. Charged particles, that only travel in water, have the dose maximum approximately at the 1D range level ($l \sim 7.5$ cm) (because the lateral straggling decreases slightly their energy). And those which have crossed the bone, have the peak around ($l \sim 7$ cm).

6 Conclusions

We have developed a fast accurate method to simulate the propagation of heavy ions. It is able to deal with very heterogeneous medium while maintaining the realizability of the solution. We dealt with the problems of a heterogeneous medium. Multi-dimensional cases are simulated and analyzed. They show the feasibility of the method. Our method's efficiency allows it to be used in a practical application context. A realizable implicit method is being developed for very low density case. This method must be as less dissipative as possible to ensure the quality of the results. Future work also include MPI massive parallelisation of the code.

We will also refine the transport coefficients. The validity of the momentum transfer coefficient can be investigated with the help of these benchmark calculations. The CSD approximation will be taken into account by using (and/or simulating) the differential cross sections of heavy ions. Secondary fragments should also be treated for heavier ions ($Z > 2$). We can also add other external forces (Lorentz force) into the code and consider the hot plasma medium.

Acknowledgements

This work was carried out by the financial support of the Agence Nationale de la Recherch (ANR-16-CE92-0027-01).

References

[1] P. Freier, E. J. Lofgren, E. P. Ney, F. Oppenheimer, H. L. Bradt, B. Peters, Evidence for heavy nuclei in the primary cosmic radiation, Phys. Rev. 74 (1948) 213.

[2] V. Tatischeff, S. Gabici, Particle acceleration by supernova shocks and spallogenic nucleosynthesis of light elements, Annual Review of Nuclear and Particle Science 68 (2018) 377–404.

[3] J. W. Wilson, S. Y. Chun, F. F. Badavi, L. W. Townsend, S. L. Lamkin, Hzetrn: A heavy ion/nucleon transport code for space radiations, Technical Report (1991).

[4] W. D. Newhauser, R. Zhang, The physics of proton therapy, Phys Med Biol. 60 (2015) R155—-R209.

[5] G. A. P. Cirrone, *et al.*, Hadrontherapy: a Geant4-based tool for proton/ion-therapy studies, Progress in nuclear science and technology 2 (2011) 207–212.

[6] E. Pedroni, *et al.*, The 200 MeV proton therapy project at the Paul Scherrer Institute: conceptual design and practical realization, Med. Phys. 22 (37) (1995).

[7] M. T. Munir, M. Federighi, Control of foodborne biological hazards by ionizing radiations, Foods 9 (7) (2020) 878.

[8] R. F. Welton, M. P. Stockli, S. N. Murray, R. Keller, The status of the spallation neutron source ion source, Review of Scientific Instruments 75 (5) (2004) 1793–1795.

[9] S. Chandrasekhar, On the radiative equilibrium of a stellar atmosphere, Astrophysical Journal 103 (1946) 351–370.

[10] S. Chandrasekhar, Radiative transfer, Courier Corporation, 2013.

[11] C. D. Levermore, Moment closure hierarchies for kinetic theories, J. Stat. Phys. 83 (1) (1996) 1021–1065.

[12] G. C. Pomraning, The equations of radiation hydrodynamics, Dover Publications Inc., 1973.

[13] B. Dubroca, J.-L. Feugeas, Hiérarchie des modèles aux moments pour le transfert radiatif, C. R. Acad. Sci. Paris 329 (10) (1999) 915–920.

[14] B. Dubroca, J.-L. Feugeas, M. Frank, Angular moment model for the fokker-planck equation, Eur. Phys. Journal D 60 (2010) 301–307.

[15] S. Guisset, S. Brull, E. d'Humières, B. Dubroca, V. Tikhonchuk, Classical transport theory for the collisional electronic M_1 model, Physica A 446 (2016) 182–194.

[16] T. Pichard, S. Brull, B. Dubroca, A numerical approach for a system of transport equations in the field of radiotherapy, Commun. Comput. Phys. 25 (4) (2019) 1097–1126.

[17] J. L. Bedfort, Calculation of absorbed dose in radiotherapy by solution of the linear boltzmann transport equations, Phys. Med. Biol. 64 (3) (2019).

[18] G. C. Pomraning, The fokker-planck operator as an asymptotic limit, Math. Models Methods Appl. Sci. 2 (1) (1992) 21–36.

[19] P. Sigmund, Stopping of Heavy Ions. A Theoretical Approach, STMP 204, Springer-Verlag Berlin Heidelberg, 2004.

[20] B. K. Srivastava, S. Mukherji, Range and stopping-power equations for heavy ions, Phys. Rev. A 14 (1976) 718–725.

[21] J. Ziegler, J. Biersack, M. Ziegler, SRIM The Stopping and Range of Ions in Matter, SRIM and Co., 2014.

[22] J. Lindhard, M. Scharff, H. E. Schiott, Range concepts and heavy ions, Mat. Phys. Medd. - K. Dan. Vid. Selsk. 33 (1) (1963).

[23] J. Biersack, J. F. Ziegler, Refined universal potentials in atomic collisions, Nucl. Inst. and Meth 194 (1982) 93–100.

[24] ICRU, International Commission on Radiation Units and Measurements, Stopping Powers and Ranges for Protons and Alpha Particles, ICRU Report 49, 1993.

[25] E. Rutherford, The scattering of α and β particles by matter and the structure of the atom, Phil. Mag. Ser. 21 (125) (1911) 669–688.

[26] L. Boltzmann, English translation: 'further studies on the thermal equilibrium of gas molecules, The Kinetic Theory of Gases. History of Modern Physical Sciences 1 (125) (2003) 262–349.

[27] A. Harten, P. Lax, B. Van Leer, On upstream differencing and Godunov type methods for hyperbolic conservation laws, SIAM review 25 (1) (1983) 35–61.

[28] E. F. Toro, Riemann Solvers and Numerical Methods for Fluid Dynamics. A Practical Introduction, Thrird edition, Springer-Verlag, Berlin, 2009.

[29] R. J. LeVeque, Finite Volume Methods for Hyperbolic Problems, Cambridge Texts in Applied Mathematics, Cambridge University Press, Cambridge, 2002.

[30] C. Berthon, Stability of the MUSCL scheme for the Euler equation, Comm. Math. Sci 3 (2) (2005) 133–157.

[31] B. Khobalatte, B. Perthame, Maximum principle on the entropy and second-order kinetic schemes, Math. of Comp. 62 (205) (1994) 119–131.

[32] C. Berthon, F. Marche, A positive preserving high order VFROE scheme for shallow water equation: a class of relaxation scheme, SIAM J. Sci Computing 30 (5) (2008) 2587–2612.

[33] GEANT4, http://www.geant4.org/geant4/.

[34] A. Sage, M. Frank, Private communication (2019).

[35] A. Gustafsson, B. K. Lind, A. Brahme, A generalized pencil beam algorithm for optimization of radiation therapy, Medical physics 21 (3) (1994) 343–356.

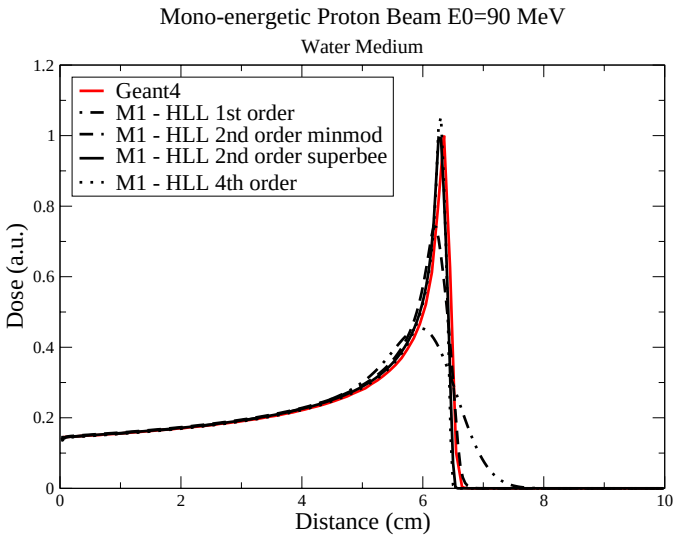

(a)

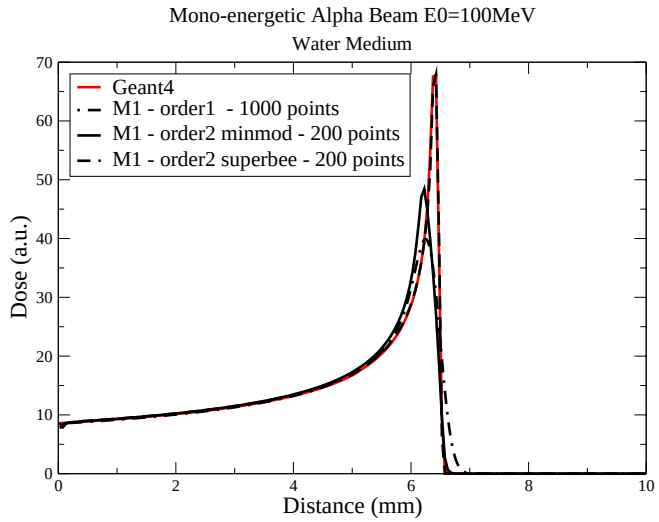

(b)

Figure 4: Comparison between a Monte Carlo code simulation (GEANT4) [33] and our M_1 code. (a) Dose of a mono-energetic ($E_0 = 90$ MeV) Proton (H^+) beam with 1st, 2nd (minmod and superbee) and 4th order schemes, (b) Dose of a mono-energetic ($E_0 = 100$ MeV) Alpha (He^+) beam with 1st, 2nd (minmod and superbee) schemes.

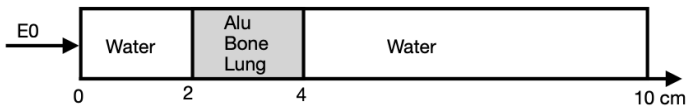

Figure 5: 1D non-homogeneous medium test-case geometry

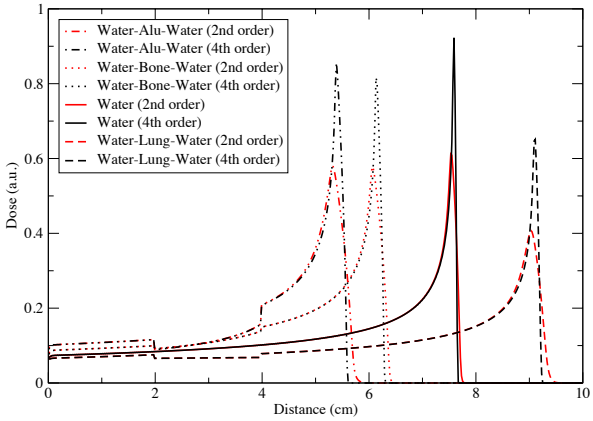

Figure 6: Dose of different cases using 2nd and 4th order schemes

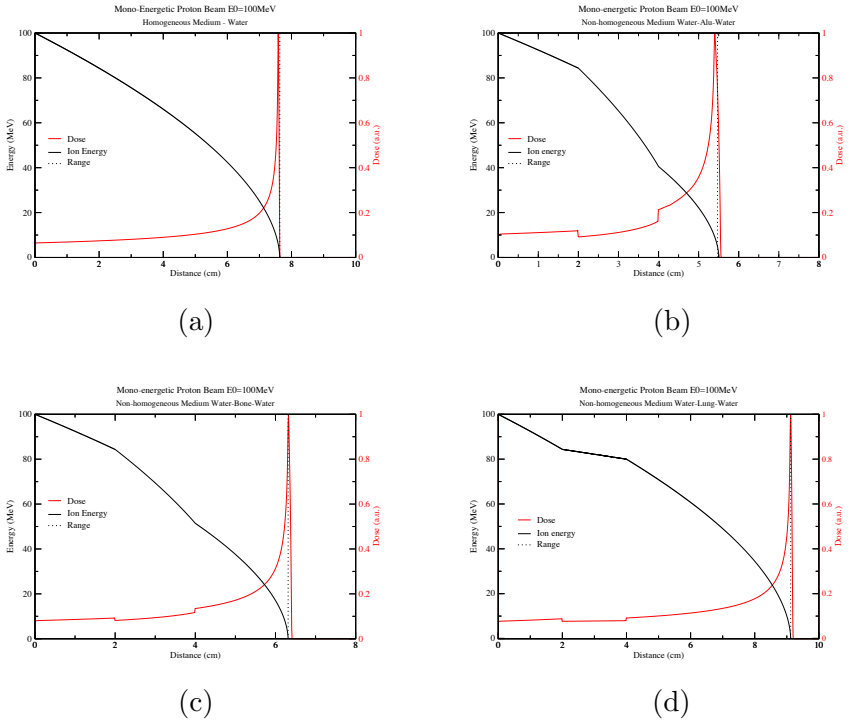

(a) (b)

(c) (d)

Figure 7: Dose and Ion Energy Path for a monoenergetic 100 MeV proton beam, (a) Homegeneous Water Medium, (b) Aluminum insert, (c) Bone insert, (d) Lung insert

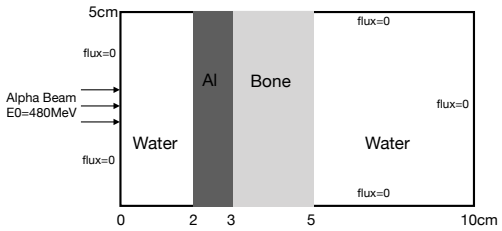

Figure 8: 2D Simulation Test Case Geometry: 1 cm 480 MeV Alpha beam from the left in the water with an aluminum insert and a bone one. Zero fluxes are imposed on the other edges.

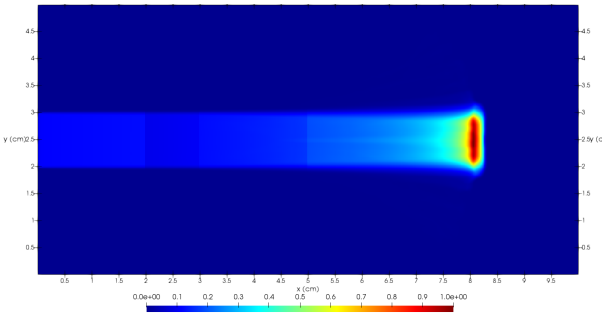

Figure 9: 2D Simulation: Dose of Alpha (He^{+}) in non-homogeneous Medium

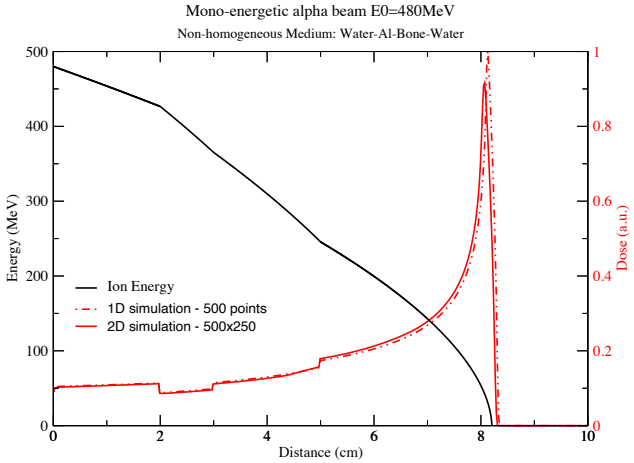

Figure 10: Comparison between 1D dose simulation (500 points, 4th order - red dotted line) and 2D dose axial distribution (500×250 points, 4th order, red solid line). 1D Ion energy path (black solid line) confirms the range value obtained by M_1 code.

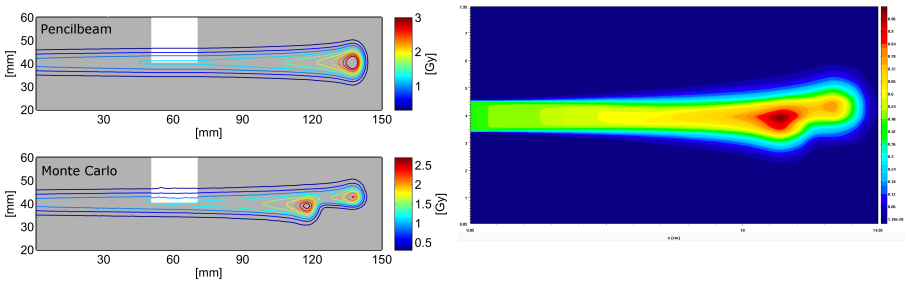

Figure 11: 2D Simulation Test-case with an air pocket: Deposited Energy by a $E_0 = 128$ MeV Proton beam in Water with an Air pocket. Comparison of M_1 simulation results of a single proton beam computed with pencil beam method and Monte Carlo code by [34].

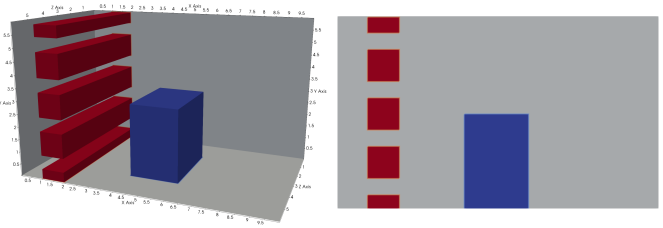

(a) (b)

Figure 12: Proton Beam in heterogeneous target : Water with Bone (red) and Lung (Navy blue) inserts. (a) 3D view, (b) 2D $xy, z = 0$ plan view

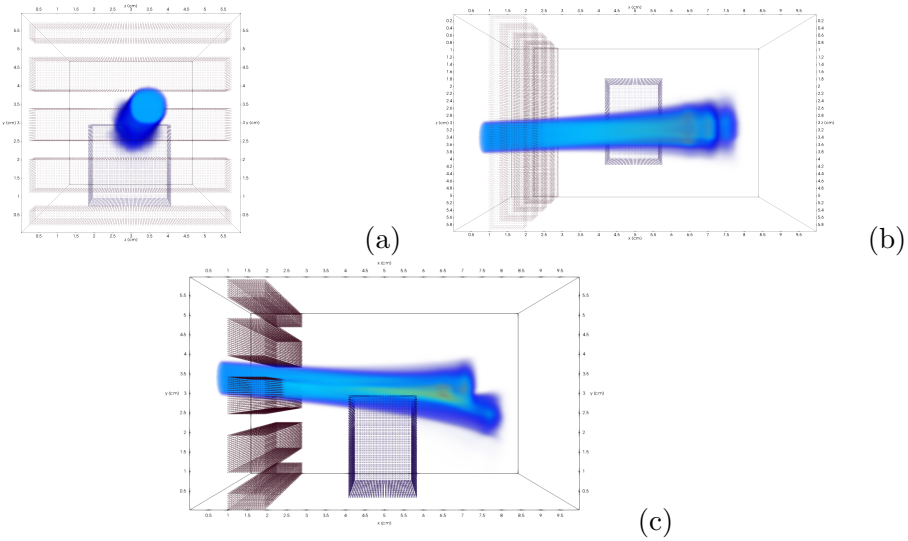

(a) (b) (c)

Figure 13: (a) View in positive x direction: $d = 1$ cm Circle Beam with inclined direction. (b) View in negative y direction: shape of the beam propagated in the medium, (c) View in negative z direction: shape of the beam propagated in the medium

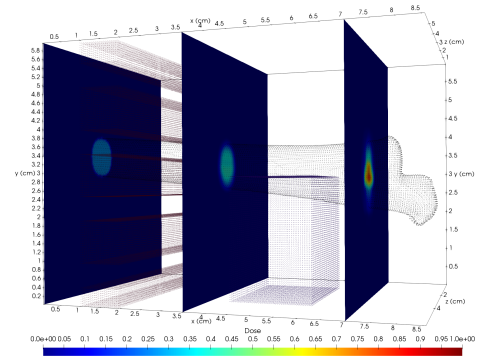

(a)

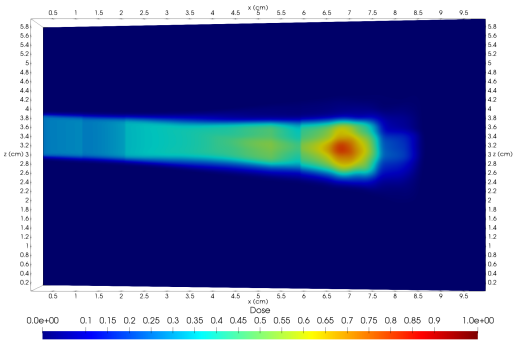

(b)

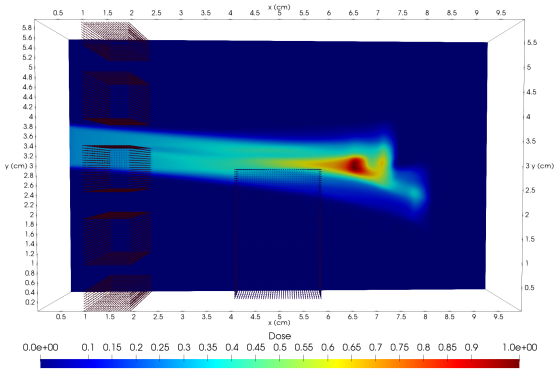

(c)

Figure 14: (a) View at planes $x = 0$, $x = 3.5$ cm, $x = 7$ cm, (b) View at plane $\mathbf{n}$=(-0.05, 0., 0.95), centered at (5,3,3), (c) View at plane $\mathbf{n}$=(0.04, 0.96, 0.), centered at (5,3,3)